

# Reflective multi-immersion microscope objectives inspired by the Schmidt telescope

Received: 20 September 2022

Accepted: 20 February 2023

Published online: 30 March 2023

 Check for updates

Fabian F. Voigt<sup>1,2,11</sup>✉, Anna Maria Reuss<sup>2,3</sup>, Thomas Naert<sup>4</sup>, Sven Hildebrand<sup>5</sup>, Martina Schaettin<sup>2,6</sup>, Adriana L. Hotz<sup>2,6</sup>, Lachlan Whitehead<sup>7,8</sup>, Armin Bahl<sup>9</sup>, Stephan C. F. Neuhauss<sup>2,6</sup>, Alard Roebroek<sup>5</sup>, Esther T. Stoeckli<sup>2,6,10</sup>, Soeren S. Lienkamp<sup>4</sup>, Adriano Aguzzi<sup>2,3</sup> & Fritjof Helmchen<sup>1,2,10</sup>

Imaging large, cleared samples requires microscope objectives that combine a large field of view (FOV) with a long working distance (WD) and a high numerical aperture (NA). Ideally, such objectives should be compatible with a wide range of immersion media, which is challenging to achieve with conventional lens-based objective designs. Here we introduce the multi-immersion ‘Schmidt objective’ consisting of a spherical mirror and an aspherical correction plate as a solution to this problem. We demonstrate that a multi-photon variant of the Schmidt objective is compatible with all homogeneous immersion media and achieves an NA of 1.08 at a refractive index of 1.56, 1.1-mm FOV and 11-mm WD. We highlight its versatility by imaging cleared samples in various media ranging from air and water to benzyl alcohol/benzyl benzoate, dibenzyl ether and ethyl cinnamate and by imaging of neuronal activity in larval zebrafish *in vivo*. In principle, the concept can be extended to any imaging modality, including wide-field, confocal and light-sheet microscopy.

Since the pioneering work by Ernst Abbe 150 years ago, many engineering innovations have improved the performance of microscope objectives<sup>1</sup>. Nonetheless, application domains exist for which better and more cost-efficient objectives still are highly desirable. One of these domains is imaging samples processed with tissue clearing techniques<sup>2,3</sup>, which render entire organs or organisms transparent while retaining fluorescent labeling. Given that, over the course of the past decade, clearing of entire mouse brains ( $\approx 1\text{ cm}^3$ ) has become routine<sup>2,4,5</sup> and that clearing of entire mice and human organs is feasible<sup>6–8</sup>, there is a need for microscope objectives that are suitable for imaging large, cleared samples at high resolution. This demand poses a challenging optical engineering problem because imaging at high resolution requires increasing the numerical aperture

(NA), which complicates the correction of aberrations and necessitates more lens elements. Beyond that, the large size of cleared samples requires objectives with long working distances (WDs), while, at the same time, large fields of view (FOVs) are necessary to allow imaging with high throughput. The most challenging engineering problem by far is, however, that published clearing protocols require immersion media with a diversity of the refractive index  $n$ , ranging from water ( $n = 1.33$ ) for expansion microscopy<sup>9</sup> to typical organic solvents such as dibenzyl ether<sup>10</sup> (DBE) or ethyl cinnamate<sup>11</sup> (ECI) with  $n = 1.56$ . Some commercial objectives have a correction collar that moves an internal lens group to minimize index-dependent aberrations, but, for high-NA objectives, designers often opt for narrowing the index range to keep the costs under control. For example, the Olympus XLSLPLN25XGMP

<sup>1</sup>Brain Research Institute, University of Zurich, Zurich, Switzerland. <sup>2</sup>Neuroscience Center Zurich, University of Zurich, Zurich, Switzerland. <sup>3</sup>Institute of Neuropathology, University Hospital Zurich, Zurich, Switzerland. <sup>4</sup>Institute of Anatomy, University of Zurich, Zurich, Switzerland. <sup>5</sup>Department of Cognitive Neuroscience, Faculty of Psychology & Neuroscience, Maastricht University, Maastricht, the Netherlands. <sup>6</sup>Department of Molecular Life Sciences, University of Zurich, Zurich, Switzerland. <sup>7</sup>Walter and Eliza Hall Institute of Medical Research, Melbourne, Victoria, Australia. <sup>8</sup>Department of Medical Biology, University of Melbourne, Melbourne, Victoria, Australia. <sup>9</sup>Centre for the Advanced Study of Collective Behaviour, University of Konstanz, Konstanz, Germany. <sup>10</sup>University Research Priority Program (URPP), Adaptive Brain Circuits in Development and Learning (AdaBD), University of Zürich, Zurich, Switzerland. <sup>11</sup>Present address: Department of Molecular and Cellular Biology, Harvard University, Cambridge, MA, USA. ✉e-mail: [fvoigt@fas.harvard.edu](mailto:fvoigt@fas.harvard.edu)

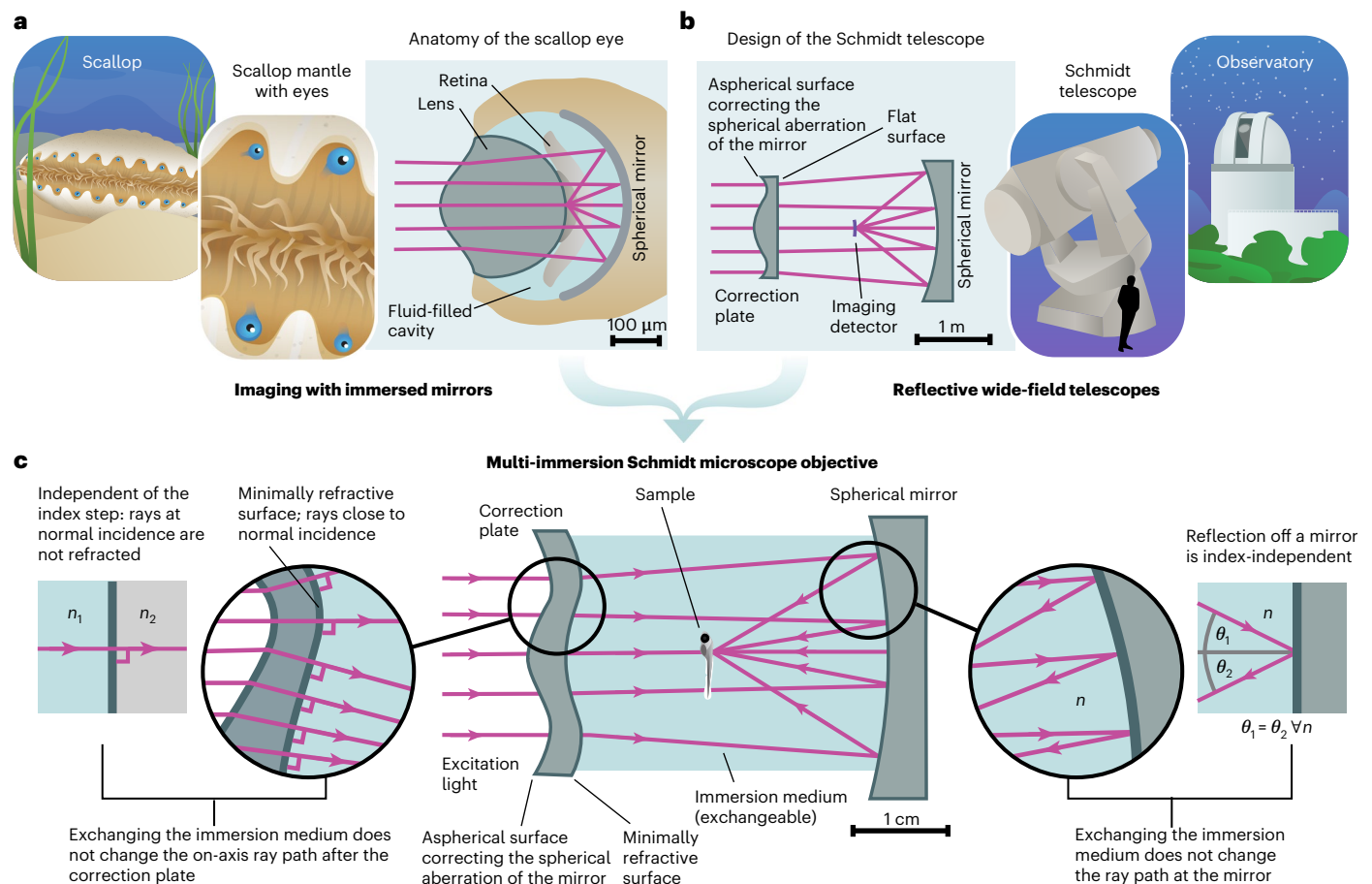


**Fig. 1 | Concept of the multi-immersion Schmidt objective.** **a**, Our approach is inspired by the anatomy of the scallop eye. In this eye design, a curved mirror in contact with a liquid forms an image on a transparent layer of photoreceptors. **b**, A second inspiration is the Schmidt telescope, a mirror-based wide-field telescope design that consists of a spherical mirror and an aspherical correction plate. **c**, We synthesize both concepts into a multi-immersion objective

design that provides a sharp image in any homogeneous medium (center). Reflection off the mirror does not depend on the refractive index  $n$  of the immersion medium (right). To avoid additional refraction at the inner surface of the correction plate, we deform this surface such that all passing rays are close to normal incidence (left).

combines NA = 1.0 with 8-mm WD but is restricted to  $n = 1.41$ – $1.52$ . Covering a larger index range is possible at the expense of resolution (for example, the Olympus XLPLN10XSVM has an NA of 0.6, 8-mm WD and  $n = 1.33$ – $1.52$ ). Such objectives typically have 13–15 lenses and are very expensive. Despite this considerable effort, indices around 1.56 are outside the specified range. And, not least, media such as DBE, ECI or benzyl alcohol/benzyl benzoate (BABB) can dissolve lens cements so that chemically resistant dipping cap designs are required. Few such options are available, of which one is an ASI/Special Optics objective (54-12-8) that covers the entire range from 1.33 to 1.56 with good chemical compatibility, featuring 10-mm WD at an NA of 0.7. However, scaling this design up to higher NA, longer WD and FOV beyond 1 mm has not been achieved so far.

To address this challenge, we introduce an approach for designing a multi-immersion objective based on a mirror instead of lenses. The underlying idea is that the reflection of a light ray by a mirror is independent of the refractive index of the medium the mirror is in contact with. Consequently, if we submerge a curved mirror inside a liquid-filled chamber and use it to focus light, the ray paths and location of the focus do not change when changing the bulk index of the immersion medium. An invariant ray path means that any monochromatic aberrations, such as spherical aberration or coma, stay constant even though the NA of the objective scales with the refractive index of the medium. This is markedly different compared to lens-based

multi-immersion designs where any medium change causes additional aberrations that need to be accounted for. In addition, reflective objective designs often have a longer WD than refractive designs at similar NA. This combination of features means that reflective optical systems are excellent templates for long-WD multi-immersion objectives. Although, to our knowledge, such a design has not been previously applied in bioimaging, it is found in nature, where each of the hundreds of eyes of scallops contains a curved mirror to form an image<sup>12</sup> (Fig. 1a). Each mirror is in direct contact with the liquid-filled space containing the photoreceptors. Each eye also contains a lens, which is not, however, the primary image-forming element<sup>13</sup>. This combination of a lens and a mirror is reminiscent of the optical design of the Schmidt telescope<sup>14</sup>, a mirror-based wide-field telescope design commonly used in astronomy since the 1930s (Fig. 1b). A Schmidt telescope is based on a spherical mirror that, as a standalone element, would create a heavily aberrated image due to spherical aberration. By adding a refractive aspherical correction plate in the center of curvature of the mirror, Bernhard Schmidt (1879–1935) created a telescope design that corrects the spherical aberration and provides excellent image quality over a large FOV. Owing to this wide-field capability, such telescopes are exceptionally well suited for surveys of the night sky. For example, the Kepler space telescope is a Schmidt telescope optimized for exoplanet detection<sup>15,16</sup>. Most Schmidt telescopes share the characteristic that, due to the rotational symmetry of the spherical mirror,

the image surface of a Schmidt telescope is curved as well. The usage of an aspherical correction plate in combination with curved mirrors forms a general solution that can be applied to a wide variety of optical design problems. Indeed, shortly after the Schmidt telescope became widely known, it was recognized that this principle could be useful to build microscope objectives<sup>17,18</sup>. However, apart from non-imaging flow cytometry<sup>19</sup>, there is no application of the Schmidt principle in modern biophotonics.

## Results

### Turning a Schmidt telescope into an immersion objective

We reasoned that it is possible to turn a Schmidt telescope into an immersion microscope objective by a series of conceptual steps (Fig. 1c and Supplementary Video 1):

1. Downscaling the design from the meter-sized apertures common in astronomy to a centimeter-sized aperture suitable for a microscope;
2. Replacing the detector in the focus of the telescope with a fluorescently labeled sample;
3. Focusing and scanning an excitation beam instead of focusing light from stars—for example, a near-infrared ultra-fast pulsed laser beam for two-photon microscopy;
4. Filling the entire inner space between the mirror and the correction plate with an immersion liquid.

We noted that this approach results in objective designs with excellent simulated image quality; however, the optimal shape of the aspherical surface correcting for spherical aberration needs to be tailored specifically to each immersion medium. Such designs with simple Schmidt correction plates are, thus, immersion objectives but not multi-immersion capable. The reason is that refraction at the interface between correction plate and immersion medium introduces additional index-dependent spherical aberration. To circumvent this problem, we make use of an edge case of the law of refraction: no matter how big the index difference at a refractive interface is, a ray at normal incidence is not refracted—that is, it does not change its propagation direction. Therefore, we additionally shape the inner surface of the correction plate such that, at all locations, the passing rays are at normal incidence. In other words, the first aspherical surface of the correction plate deforms the incoming parallel wavefront to counteract the spherical aberration of the spherical mirror, and the second surface is then shaped exactly like this deformed wavefront. As the wavefront passes the interface unchanged, no additional (index-dependent) aberrations are introduced. We refer to this interface as a ‘minimally refractive’ surface because it does not have any net refractive power. Because in typical laser scanning microscopes the scan angles at the objective are usually only a few degrees, even off-axis ray bundles strike the minimally refractive surface at near-normal incidence, which allows the design to have millimeter-sized FOVs. We term the resulting multi-immersion Schmidt-telescope-turned microscope objective a ‘Schmidt objective’.

### Design of a multi-photon Schmidt objective

Although our concept can be used to design objectives for a wide variety of imaging modalities, we opted to demonstrate the design as a multi-photon objective. The reason is that many multi-photon techniques, such as two-photon microscopy, require only a single laser source, and the excitation spectrum is so narrow that no color correction is necessary, and, due to non-descanned detection, the collection path does not have to be color-corrected. Consequently, the design can be kept extremely simple: our multi-photon objective design has only two optical elements and can be used with a tunable ultrafast excitation laser in the 750–1,000-nm range. Owing to the reflective geometry, the sample sits in between the mirror and the correction plate. Therefore, we define the working distance as the axial spacing between the focus and the outer rim of the mirror because this is the feasible z-range

before a sample holder would collide with the mirror (Extended Data Fig. 1a). For our Schmidt objective, this working distance is 11 mm. As the on-axis ray path is independent of the refractive index of the immersion medium, the NA scales linearly with  $n$ , and no correction collar is required. In air and using 800-nm excitation light, the design has an NA of 0.69 and a diffraction-limited field of view (dFOV) of 1.6 mm diameter (Extended Data Fig. 1b). The system has an index-independent entrance pupil diameter of 22 mm. As a result, the etendue (or optical invariant of the system) is constant, and the product of NA and FOV is invariant as well. Consequently, in a higher-index medium such as water, the NA increases to 0.92, but the dFOV decreases to 1.4 mm. For typical organic solvents, such as ECI, DBE or BABB with an index of 1.56, the NA reaches 1.08, and the dFOV is 1.1 mm. The focal surface of the Schmidt objective is curved with a radius of 15.68 mm. Supplementary Note 1 provides an overview of the theory underlying our design approach. To turn this design into a prototype, we designed an immersion chamber around the optical components of the objective and integrated it into a custom horizontal multi-photon microscope (Fig. 2a–c). We chose a horizontal setup as it makes the exchange of immersion media and samples straightforward. In our prototype, the mirror is attached to a motorized  $x$ – $y$ – $z$  stage and needs to be aligned relative to the correction plate. We opted for this approach because, initially, it was unclear how often the mirror would require cleaning and possibly replacement due to damaged coatings. In practice, however, we did not observe any coating damage even after prolonged immersion of the mirror in imaging media, such as DBE, BABB or ECI (Supplementary Note 1). This means that future Schmidt objectives can be designed with a mirror that is fixed in the immersion chamber.

### Characterization of the multi-photon Schmidt objective

We characterized the optical resolution of the objective by imaging 200-nm fluorescent beads at 800-nm excitation wavelength (Fig. 2d,e). In air (NA = 0.69), we measured an on-axis point spread function (PSF) with a full width at half maximum (FWHM) of  $0.56 \pm 0.01 \mu\text{m}$  in  $x$  (mean  $\pm$  s.e.m.),  $0.49 \pm 0.07 \mu\text{m}$  in  $y$  and  $1.93 \pm 0.01 \mu\text{m}$  in  $z$  ( $n = 8$  beads). In water, the PSF size decreased to  $0.42 \pm 0.04 \mu\text{m}$  in  $x$ ,  $0.43 \pm 0.03 \mu\text{m}$  in  $y$  and  $1.65 \pm 0.1 \mu\text{m}$  in  $z$  ( $n = 8$  beads). When filling the objective with an immersion oil with  $n = 1.45$ , the PSF size further decreased to  $0.36 \pm 0.01 \mu\text{m}$  in  $x$ ,  $0.33 \pm 0.01 \mu\text{m}$  in  $y$  and  $1.33 \pm 0.09 \mu\text{m}$  in  $z$  ( $n = 8$  beads). Further increasing the index to  $n = 1.51$  led to PSF size of  $0.36 \pm 0.02 \mu\text{m}$  in  $x$ ,  $0.32 \pm 0.02 \mu\text{m}$  in  $y$  and  $1.36 \pm 0.01 \mu\text{m}$  in  $z$  ( $n = 8$  beads). Across the index range, the on-axis PSF sizes were similar to diffraction-limited values<sup>20</sup>. Imaging parameters are listed in Supplementary Table 1. According to our simulations (Extended Data Fig. 1b–d), our objective supports a diffraction-limited FOV of 1.7 mm in air, 1.4 mm in water and 1.1 mm at  $n = 1.56$ . Due to additional off-axis aberrations introduced by our scan and tube lens, the whole system is diffraction limited only up to a maximum scan angle of  $\pm 1.75^\circ$ , which corresponds to a dFOV of 0.74 mm in air, 0.68 mm in water and 0.54 mm at  $n = 1.56$  (Extended Data Fig. 1e–g). Therefore, we characterized the PSFs at a scan angle of  $\pm 1.75^\circ$  (Fig. 2e and Extended Data Fig. 2) and found that the off-axis PSFs are in good agreement with our simulations.

### Imaging examples using the Schmidt objective

To demonstrate the imaging capabilities of our Schmidt objective, we imaged both cleared and living samples (Fig. 3). In cleared samples, we first acquired low-resolution overview datasets with a mesoSPIM<sup>21</sup> single-photon light-sheet microscope before transferring the sample into the Schmidt objective for high-resolution imaging. To showcase that the objective can be used in air, we imaged a pollen pellet composed of many individual pollen grains (Fig. 3a). At higher zoom levels, surface features on individual pollen grains become readily apparent. Because the Schmidt objective is a multi-immersion objective, we could then fill the immersion chamber with ECI ( $n = 1.56$ ) and image the same pollen grains in this high-index medium (Extended Data Fig. 3).

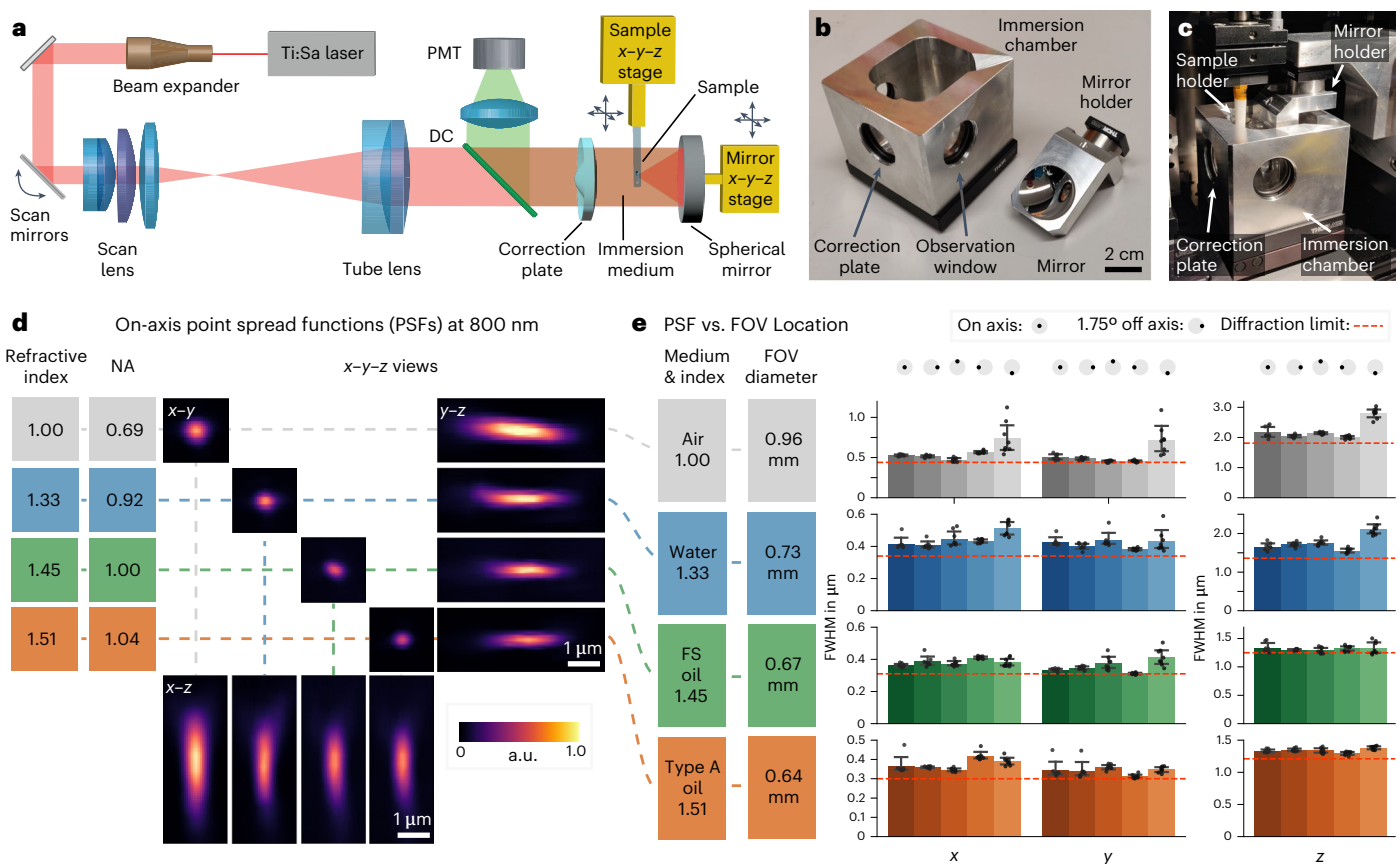


**Fig. 2 | Setup and characterization.** **a**, Overview of the multi-photon microscopy setup. In our prototype, the position of the spherical mirror needs to be aligned relative to the correction plate for optimum image quality. This design allows for straightforward cleaning of the mirror when switching immersion media. To create a z-stack, the sample is moved along the optical axis. DC indicates a dichroic mirror that separates the emitted fluorescence from the excitation beam. **b**, The prototype objective consists of an immersion chamber and a mirror. **c**, Assembled microscope objective. **d**,  $x$ - $y$ - $z$  views of PSF measurements of 200-nm fluorescent beads imaged at refractive indices ranging from  $n = 1.00$  (air),  $n = 1.33$  (water) and  $n = 1.45$  (FS, Cargille fused silica matching oil) to

$n = 1.51$  (Cargille oil type A). Because NA is proportional to  $n$ , an increase in  $n$  leads to higher NA and, thus, a smaller PSF. **e**, PSF uniformity over the FOV. PSF measurements were carried out on-axis and at a scan angle of  $1.75^\circ$ , which was simulated to be the maximum theoretical diffraction-limited scan angle for the total system (Extended Data Fig. 1). As the magnification of the objective is proportional to  $n$ , the FOV diameter decreases with increasing index. Diffraction-limited theoretical values are indicated by the red dashed lines. The PSF FWHM ( $\pm$ s.e.m.) was measured for eight beads for each FOV location and immersion medium. a.u., arbitrary units.

Next, we placed a 5-day-old larval zebrafish expressing the calcium indicator GCaMP6s in neurons in the Schmidt objective and filled it with fish water ( $n = 1.33$ ). We acquired stacks of the entire zebrafish brain and were able to record neuronal activity in the tectum (Fig. 3b). To illustrate that the objective can be used for imaging cleared samples, we imaged 3-day-old *Xenopus tropicalis* tadpoles in BABB ( $n = 1.56$ ), visualizing their developing nervous system and their retinal photoreceptor layer (Fig. 3c and Supplementary Video 2). It was also possible to perform second-harmonic generation (SHG) imaging of muscle fibers in a tadpole embryo tail, resolving individual sarcomeres (Extended Data Fig. 4). We also applied the Schmidt objective to image larger cleared embryos in BABB—for example, a 4-day-old chicken embryo, which is about 6 mm in size (Extended Data Fig. 5 and Supplementary Video 3). Next, we replaced the immersion medium with DBE (also  $n = 1.56$ ) and inserted a 4-mm-thick coronal slice of an iDISCO-processed<sup>4</sup> Thy1-YFP-H mouse brain. In this sample, we were able to visualize spines along apical dendrites (Fig. 3d). We also successfully imaged dopaminergic neurons in a sample from a mouse brain stained for tyrosine hydroxylase (Extended Data Fig. 6). Finally, we acquired a dataset from a MASH-processed<sup>22</sup>  $5 \times 7 \times 4$ -mm<sup>3</sup> piece of human neocortex in ECI, enabling us to visualize neuronal somata and the dense neuropil (Fig. 3e).

## Discussion

Taken together, these examples illustrate how a single Schmidt objective, owing to its large index range, covers a range of applications that would usually require several objectives. Despite having only three optical surfaces, our design outperforms all existing commercial multi-photon microscope objectives for cleared tissue within the parameter space of WD, index range, maximum NA and FOV (Extended Data Fig. 7). Whereas our mirror-based design provides multi-immersion capability basically for free, the reflective ray path means that the objective surrounds the sample, which is similar to light-sheet microscopes for which custom sample holders and mounting techniques are often necessary. In addition, the bigger the sample is, the more it obstructs the excitation path, which can lead to diffraction artifacts. In our prototype, we used samples up to 5 mm in diameter without a severe loss in image quality (Extended Data Fig. 5). Scaling up the entire objective will allow bigger samples, such as entire mouse brains, to be accommodated. It is also possible to design unobstructed off-axis Schmidt objectives that would allow samples of arbitrary lateral size to be imaged. Similarly to a Schmidt telescope, we allow the focal surface to be curved, which did not turn out to be an issue when imaging three-dimensional samples because the  $z$ -shift across the FOV is small (that is,  $\Delta z = 1.2 \mu\text{m}$  across

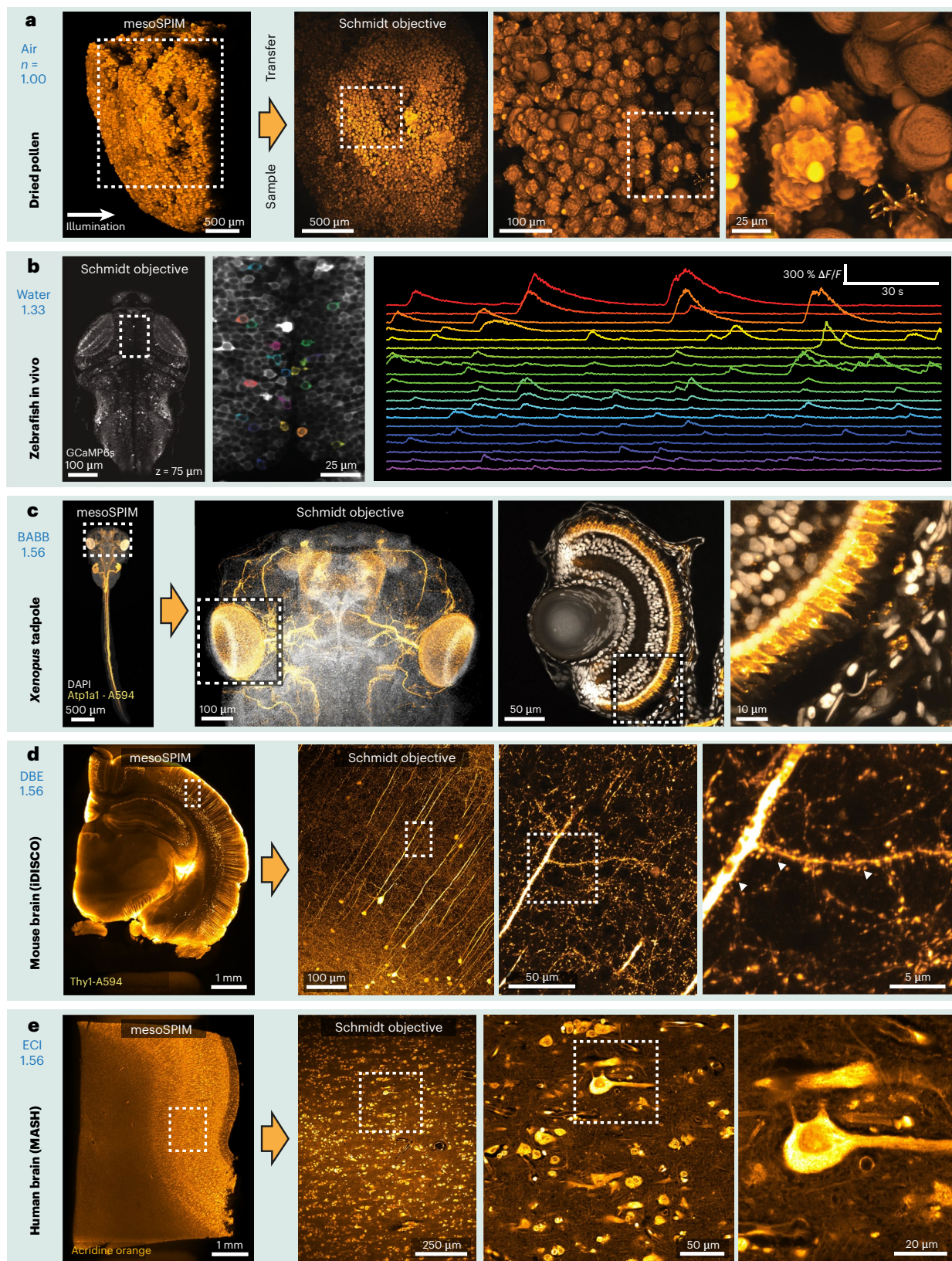


**Fig. 3 | Example two-photon datasets acquired with the Schmidt objective.** Fixed samples were first imaged with a mesoSPIM light-sheet microscope before the sample was transferred to the Schmidt objective. **a**, Pollen pellet composed of many individual pollen grains imaged in air. **b**, Functional imaging in a 5-day-old *elavl3:GCaMP6s* zebrafish larva in vivo (example dataset from one of three imaged larvae). **c**, BABB-cleared *X. tropicalis* tadpole stained for Atp1a1 (Alexa Fluor 594, orange) and nuclei (DAPI, grayscale). The large Schmidt FOV allows

both imaging of the entire head ( $\approx 800$   $\mu\text{m}$  across) and imaging of individual developing photoreceptors in the eye (right). The images are examples from one of four imaged tadpoles. **d**, Thy1-H-labeled coronal mouse brain slice imaged in DBE. At higher magnification, spines on apical dendrites of L5 neurons are visible. The images are examples from one of two imaged mouse brain slices. **e**, MASH-processed human neocortex stained with acridine orange. The images are examples from one of two imaged samples.

a 400- $\mu\text{m}$  FOV). The long path length inside the immersion medium means that the image quality depends on the homogeneity of the liquid. As a consequence, we could not achieve satisfactory image quality in CLARITY samples because the required refractive index matching solutions were not homogeneous enough, whereas imaging in organic solvents was straightforward. This property is not specific to the Schmidt objective, however: any immersion objective with long WD and high NA will show similar behavior. We foresee that the ongoing development of clearing techniques for larger and larger samples will naturally converge toward highly homogeneous imaging media as they provide the best imaging results independent of the microscopy modality. To further improve image quality, it is possible to combine the Schmidt objective with adaptive optics. Owing to their low dispersion and large wavelength range, reflective objectives have previously been used for multi-photon microscopy<sup>23,24</sup> but not as fully immersed systems. We think that our work opens an unexplored design space for building immersion microscope objectives. In principle, our concept can be extended to any imaging modality, including wide-field, confocal and light-sheet microscopy. The underlying simplicity of the concept makes it well suited for low-cost objectives that can be mass produced for diagnostic applications. Additionally, in optical design, simplicity begets scalability. Our approach will likely allow the design of ‘mesoscope objectives’ that perform high-resolution (NA > 1) imaging across centimeter-scale FOVs and are capable of extremely high-throughput imaging<sup>25–27</sup> (Supplementary Table 2). We think that the most promising imaging modality for future multi-immersion Schmidt objectives is light-sheet microscopy. To realize this promise, two challenges must be addressed. First, better chromatic correction across a wide range of immersion media with varying dispersion is necessary because our current design is not achromatic as required for single-photon imaging of fluorophores with broad emission spectra. Second, the field curvature of the Schmidt objective needs to be minimized or the light sheet needs to have a matching curvature. In principle, the latter could be achieved using curved Bessel-like excitation beams<sup>28</sup>. Addressing both challenges would open new avenues for future multi-immersion light-sheet microscopes to realize the potential of existing imaging sensors with more than 100 megapixels. Beyond that, our development of the Schmidt objective shows that astronomers and microscopists might benefit from closer interactions. In this regard, our work lends credence to a remark that Victor Hugo made in *Les Misérables* in 1862: ‘Where the telescope ends the microscope begins, and who can say which of the two provides the grander view? Choose’.

## Online content

Any methods, additional references, Nature Portfolio reporting summaries, source data, extended data, supplementary information, acknowledgements, peer review information; details of author contributions and competing interests; and statements of data and code availability are available at <https://doi.org/10.1038/s41587-023-01717-8>.

## References

- Zhang, Y. & Gross, H. Systematic design of microscope objectives. Part I: system review and analysis. *Adv. Opt. Technol.* **8**, 313–347 (2019).
- Chung, K. et al. Structural and molecular interrogation of intact biological systems. *Nature* **497**, 332–337 (2013).
- Richardson, D. S. et al. Tissue clearing. *Nat. Rev. Methods Primers* **1**, 84 (2021).
- Renier, N. et al. iDISCO: a simple, rapid method to immunolabel large tissue samples for volume imaging. *Cell* **159**, 896–910 (2014).
- Susaki, E. A. et al. Whole-brain imaging with single-cell resolution using chemical cocktails and computational analysis. *Cell* **157**, 726–739 (2014).
- Pan, C. et al. Shrinkage-mediated imaging of entire organs and organisms using uDISCO. *Nat. Methods* **13**, 859–867 (2016).
- Cai, R. et al. Panoptic imaging of transparent mice reveals whole-body neuronal projections and skull–meninges connections. *Nat. Neurosci.* **22**, 317–327 (2019).
- Zhao, S. et al. Cellular and molecular probing of intact human organs. *Cell* **180**, 796–812 (2020).
- Chen, F., Tillberg, P. W. & Boyden, E. S. Expansion microscopy. *Science* **347**, 543–548 (2015).
- Ertürk, A. et al. Three-dimensional imaging of solvent-cleared organs using 3DISCO. *Nat. Protoc.* **7**, 1983–1995 (2012).
- Klingberg, A. et al. Fully automated evaluation of total glomerular number and capillary tuft size in nephritic kidneys using lightsheet microscopy. *J. Am. Soc. Nephrol.* **28**, 452–459 (2017).
- Land, M. F. Image formation by a concave reflector in the eye of the scallop, *Pecten maximus*. *J. Physiol.* **179**, 138–153 (1965).
- Palmer, B. A. et al. The image-forming mirror in the eye of the scallop. *Science* **358**, 1172–1175 (2017).
- Schmidt, B. Ein lichtstarkes komafreies Spiegelsystem. *Mitteilungen der Hamburger Sternwarte in Bergedorf* **7**, 17 (1938).
- Borucki, W. J. et al. Kepler planet-detection mission: introduction and first results. *Science* **327**, 977–980 (2010).
- Koch, D. G. et al. Kepler mission design, realized photometric performance, and early science. *Astrophys. J.* **713**, L79–L86 (2010).
- Hendrix, D. O. & Christie, W. H. Some applications of the Schmidt principle in optical design. *Sci. Am.* **161**, 118–123 (1939).
- Bouwens, A. *Achievements in Optics* (Elsevier, 1950).
- Brittain, G. C. et al. A novel semiconductor-based flow cytometer with enhanced light-scatter sensitivity for the analysis of biological nanoparticles. *Sci. Rep.* **9**, 16039 (2019).
- Zipfel, W., Williams, R. & Webb, W. Nonlinear magic: multiphoton microscopy in the biosciences. *Nat. Biotechnol.* **21**, 1369–1377 (2003).
- Voigt, F. F. et al. The mesoSPIM initiative: open-source light-sheet microscopes for imaging cleared tissue. *Nat. Methods* **16**, 1105–1108 (2019).
- Hildebrand, S., Schueth, A., Herrler, A., Galuske, R. & Roebroek, A. Scalable labeling for cytoarchitectonic characterization of large optically cleared human neocortex samples. *Sci. Rep.* **9**, 10880 (2019).
- Amirsolaimani, B., Cromey, B., Peyghambarian, N. & Kieu, K. All-reflective multiphoton microscope. *Opt. Express* **25**, 23399–23407 (2017).
- Kabir, M. M., Choubal, A. M. & Toussaint, K. C. Jr. Application of a reflective microscope objective for multiphoton microscopy. *J. Microsc.* **271**, 129–135 (2018).
- McConnell, G. et al. A novel optical microscope for imaging large embryos and tissue volumes with sub-cellular resolution throughout. *eLife* **5**, e18659 (2016).
- Fan, J. et al. Video-rate imaging of biological dynamics at centimetre scale and micrometre resolution. *Nat. Photonics* **13**, 809–816 (2019).
- Keller, P. J., Flickinger, D. A. & Wang, B. Catadioptric microscopy. US patent application 20230003987 (2023).
- Chremmos, I. D., Chen, Z., Christodoulides, D. N. & Efremidis, N. K. Bessel-like optical beams with arbitrary trajectories. *Opt. Lett.* **37**, 5003–5005 (2012).

**Publisher’s note** Springer Nature remains neutral with regard to jurisdictional claims in published maps and institutional affiliations.

**Open Access** This article is licensed under a Creative Commons Attribution 4.0 International License, which permits use, sharing, adaptation, distribution and reproduction in any medium or format,

as long as you give appropriate credit to the original author(s) and the source, provide a link to the Creative Commons license, and indicate if changes were made. The images or other third party material in this article are included in the article's Creative Commons license, unless indicated otherwise in a credit line to the material. If material is not included in the article's Creative Commons license and your intended

use is not permitted by statutory regulation or exceeds the permitted use, you will need to obtain permission directly from the copyright holder. To view a copy of this license, visit <http://creativecommons.org/licenses/by/4.0/>.

© The Author(s) 2023

## Methods

### Objective design

The objective was designed using Zemax 2010 and Zemax OpticStudio 18. The aspherical correction plate was manufactured according to custom specifications out of fused silica by Asphericon Jena. The spherical mirror with 30-mm diameter was manufactured out of fused silica (Corning, 7980) and coated with aluminium and a protective layer of SiO<sub>2</sub> (Prazisionsoptik Gera). The design process is described in Supplementary Note 1. For imaging in liquid media, the objective was filled with 65 ml of immersion medium.

### Setup

Excitation light from a tunable femtosecond Ti:Sapphire laser (Chameleon Ultra II, Coherent) was sent through a Pockels cell (model 350-80 with 302RM controller, Conoptics) and expanded using a ×6 Galilean telescope composed of a −25-mm and a 150-mm achromat (ACN127-25B and AC254-150B-ML, Thorlabs). The beam was then routed to a pair of 10-mm galvo mirrors (6220H, Cambridge Technology) and directed through a 4f system composed of an  $f = 89$  mm scan lens (S4LFT0089/92, Sill Optics) and an  $f = 300$  mm tube lens (88-597, Edmund Optics) to the objective. The galvos could be replaced by a resonant scanner/8-mm galvo pair (CRS4K and 6220H, Cambridge Technology) for fast imaging. Emission light was separated from the excitation beam using a NIR/VIS dichroic (HC 705 LP, AHF) and collected onto two GaSP photomultipliers (HI0771P-40 SEL, Hamamatsu) by a ×4.7 demagnifying telescope composed of an  $f = 90$  mm achromat (G322389000, Qioptiq) and a wide-angle eyepiece (Panoptic 19 mm, TeleVue) as previously described<sup>29</sup>. Custom interchangeable filter cubes allowed the selection of emission channels. In addition, a 720-nm short-pass filter (ET720SP, AHF) located in front of the photomultiplier tube (PMT) blocked unwanted excitation light. PMT signals were amplified and low-pass filtered by a transimpedance amplifier (DHPCA-100 set to 14-MHz bandwidth, 105 V/A gain, Femto). The amplified signal was digitized by an NI-5734 DAQ card connected to an NI-7961R FPGA (both National Instruments). Scanning waveforms were generated using NI-6341 cards in a PXIe-1073 chassis (National Instruments). ScanImage 2017b12 (Vidrio Technologies) running on MATLAB 2019b (MathWorks) was used to control image acquisition. The sample was moved in  $x$ - $y$ - $z$  by an MP130-50-DC-L100 stage with linear encoders (Steinmayer Mechatronik) controlled by a Galil DMC-2132 motor controller. An additional rotation stage (PRMLZ8 with KDC101 controller, Thorlabs) allowed sample rotation. A second MP130 stage allowed  $x$ - $y$ - $z$  translation of the spherical objective mirror. Both mirror and sample were quick-exchangeable using kinematic magnetic mounts (KB25/M, Thorlabs).

### PSF measurements

Sample holders for fluorescent beads were built by gluing smaller coverslips (3 mm  $\varnothing$ , CS-3R-0, Warner Instruments) to a 2-mm glass capillary tube (Harvard Apparatus) using silicone adhesive (Würth, Super RTV Silikon). Fluoresbrite YG Microspheres (0.20  $\mu$ m size, Polysciences) were diluted in distilled water and pipetted on the coverslip. The capillary tube was clamped into a sample holder and inserted into the Schmidt objective. For imaging at an index of  $n = 1.45$ , the immersion chamber was filled with a fused silica matching liquid (50350, Cargille). Type A immersion oil (16482, Cargille) was used for measurements at  $n = 1.51$ . The liquids were chosen such that the fluorescent beads did not dissolve; other immersion media, such as BABB, DBE and ECI, rapidly dissolved Fluoresbrite beads. For each immersion medium and FOV location, eight beads were measured, and the resulting PSFs were fitted with Gaussian profiles in  $x$ - $y$ - $z$ .

### Imaging pollen grains

We glued a pollen granule sold as nutritional supplement (Morga Bluetenpollen, Morga AG) to a 2-mm borosilicate glass tube (TG200-4,

Harvard Apparatus) with Super RTV Silicone Transparent (Würth). The dried granules were usually composed of a single type of pollen grain and could be pre-selected for shape and fluorescence under a wide-field microscope. We selected a pollen granule with spikes (echinate sculptures). Immersing pollen granules in water or other polar solvents dissolves them into single pollen, which is why we used ECI to image pollen granules in high refractive index medium in addition to imaging them in air.

### Functional imaging of larval zebrafish

We generated larvae by incrossing adult transgenic *elavl3:GCaMP6s* fish<sup>30</sup>. Small groups of  $\approx 20$  larvae were raised in filtered fish water in 10-cm Petri dishes on a 14-hour light, 10-hour dark cycle at constant 28 °C. For imaging, larvae with strong GCaMP6s fluorescence and no pigmentation (*mitfa*<sup>-/-</sup>) were selected. Larvae were embedded in 2% agarose (UltraPure Low Melting Point Agarose, 16520-100, Invitrogen) before imaging. We estimated that 33 mW of laser power was used for imaging (Supplementary Note 1 and Supplementary Table 1).

This set of animal experiments and procedures was performed in accordance with standard ethical guidelines and was approved by the Cantonal Veterinary Office of the Canton of Zurich.

### iDISCO staining and clearing of mouse brains

Mouse experiments and procedures were performed in accordance with standard ethical guidelines and were approved by the Cantonal Veterinary Office of the Canton of Zurich. Mouse brain chunks were stained for neurons and cleared using a modified version of the iDISCO protocol<sup>4</sup>. C57BL6/J wild-type and Thy1-YFP HJrs/J transgenic (Jackson, 003782) mice aged 4 weeks and 17 weeks, respectively, were anesthetized and perfused, and the brains were post-fixed in 4% paraformaldehyde (PFA) in PBS for 4.5 hours at 4 °C, shaking at 40 r.p.m. Mouse brains were washed in PBS for 3 days at room temperature and 40 r.p.m., with daily solution exchange. Samples were cut into 5-mm<sup>3</sup> chunks and dehydrated in serial incubations of 20%, 40%, 60% and 80% methanol (MeOH) in ddH<sub>2</sub>O, followed by two times 100% MeOH, each for 1 hour at room temperature and 40 r.p.m. Pre-clearing was performed in 33% MeOH in dichloromethane (DCM) overnight at room temperature and 40 r.p.m. After two times washing in 100% MeOH, each for 1 hour at room temperature and then 4 °C at 40 r.p.m., bleaching was performed in 5% hydrogen peroxide in MeOH for 20 hours at 4 °C and 40 r.p.m. Samples were rehydrated in serial incubations of 80%, 60%, 40% and 20% MeOH in ddH<sub>2</sub>O, followed by PBS, each for 1 hour at room temperature and 40 r.p.m. Permeabilization was performed by incubating the samples two times in 0.2% Triton X-100 in PBS, each for 1 hour at room temperature and 40 r.p.m., followed by incubation in 0.2% Triton X-100 + 10% dimethyl sulfoxide (DMSO) + 2.3% glycine + 0.1% sodium azide (NaN<sub>3</sub>) in PBS for 5 days at 37 °C and 65 r.p.m. Blocking was performed in 0.2% Tween 20 + 0.1% heparine (10 mg ml<sup>-1</sup>) + 5% DMSO + 6% donkey serum in PBS for 2 days at 37 °C and 65 r.p.m. Samples were stained gradually with polyclonal rabbit-anti-tyrosine hydroxylase antibody (Sigma-Aldrich, AB152) 1:200 or polyclonal chicken-anti-GFP antibody (Aves Labs, GFP-1020) 1:400, followed by secondary donkey-anti-rabbit-Alexa Fluor 594 antibody (Thermo Fisher Scientific, A32754) 1:200 or donkey-anti-chicken-Alexa Fluor 594 antibody (Jackson ImmunoResearch, 703-585-155) 1:400 in 0.2% Tween 20 + 0.1% heparine + 5% DMSO + 0.1% NaN<sub>3</sub> in PBS (staining buffer) in a total volume of 1.5 ml per sample every week for 2 weeks at 37 °C and 65 r.p.m. Washing steps were performed in staining buffer five times each for 1 hour and then for 2 days at room temperature and 40 r.p.m. Clearing was started by dehydrating the samples in serial MeOH incubations as described above. Delipidation was performed in 33% MeOH in DCM overnight at room temperature and 40 r.p.m., followed by two times 100% DCM each for 15 minutes at room temperature and 40 r.p.m. Refractive index matching was achieved in DBE ( $n = 1.56$ ) for 4 hours at room temperature.



### Staining and clearing of *Xenopus* embryos

Whole-mount immunofluorescence procedures were adapted from previously described protocols<sup>31,32</sup>. All experiments were performed in accordance with standard ethical guidelines and were approved by the Cantonal Veterinary Office of the Canton of Zurich. Embryos were fixed at Nieuwkoop/Faber stage 42 for 40 minutes at room temperature in 4% PFA. Embryos were rinsed three times with 1× PBS, dehydrated to 100% MeOH and stored overnight at −20 °C. Bleaching was performed at room temperature shaking under strong light in 10% H<sub>2</sub>O<sub>2</sub>/23% H<sub>2</sub>O/66% MeOH for 48 hours. Embryos were rehydrated to 1× PBS with 0.1% Triton X-100 (PBT), and blocking was performed for 2 hours in 10% CAS-Block/90% PBT (Life Technologies). Staining was performed using the Atp1a1 antibody (1:200, DSHB, A5) diluted in 100% CAS-Block for 48 hours at 4 °C. For nuclear counterstaining, DAPI (20 µg ml<sup>−1</sup>, Thermo Fisher Scientific, D1306) was added to the primary antibody mixture. Embryos were washed for 3 × 30 minutes with PBT, blocked again for 2 hours (10% CAS-Block/90% PBT) and incubated overnight at 4 °C with secondary antibody (1:250, Alexa Fluor 594, Thermo Fisher Scientific, A32742) diluted in 100% CAS-Block. Embryos were washed for 2 × 1 hour with PBT and then 1 hour in PBS. Embryos were embedded in 2% low-melting agarose and dehydrated as follows: 25% MeOH/75% 1× PBS (2 hours), 50% MeOH/50% 1× PBS (2 hours), 75% MeOH/25% 1× PBS (2 hours) and three times 100% MeOH (2 × 45 minutes, 1× overnight). Clearing was performed in BABB (benzyl alcohol:benzyl benzoate 1:2) overnight.

### Neurofilament staining of a whole-mount chicken embryo

The embryo was sacrificed at day 4 of development and incubated in 4% PFA for 2 hours at room temperature. For best staining and clearing results, the embryo was kept in constant, gentle motion throughout the staining procedure. Incubation was at 4 °C. The tissue was permeabilized in 0.5% Triton X-100/PBS for 1 hour, followed by an incubation in 20 mM lysine in 0.1 M sodium phosphate pH 7.3 for 1 hour. In a next step, the embryo was rinsed with five changes of PBS. Non-specific binding was blocked using 10% FCS in PBS for 1 hour. The primary antibody mouse anti-neurofilament (1:2,000, RMO270, Invitrogen, 13-0700) was added for 48 hours. The primary antibody was removed, and the tissue was rinsed with ten changes of PBS and an additional incubation overnight. After re-blocking in FCS/PBS for 1 hour, the embryo was incubated with the secondary antibody goat-anti-mouse IgG-Alexa Fluor 568 (1:1,000, Jackson ImmunoResearch, 115-165-003) for 15 hours. Then, the embryo was washed ten times with PBS, followed by incubation overnight in PBS. For imaging, the tissue was dehydrated in a methanol gradient (25%, 50% and 75% in ddH<sub>2</sub>O and 2 × 100%, 1 hour each step) and cleared using 1:2 benzyl alcohol:benzyl benzoate (BABB) solution overnight (again, gentle shaking is recommended for dehydration and clearing). The tissue and staining are stable for months when kept at 4 °C in the dark. This set of animal experiments and procedures was performed in accordance with standard ethical guidelines and was approved by the Cantonal Veterinary Office of the Canton of Zurich.

### Human brain tissue preparation

The human occipital lobe samples were obtained from the body donation program of the Department of Anatomy and Embryology at Maastricht University. The tissue donor gave their informed and written consent to the donation of their body for teaching and research purposes as regulated by the Dutch law for the use of human remains for scientific research and education ('Wet op de Lijkbezorging'). Accordingly, a handwritten and signed codicil from the donor posed when still alive and well is kept at the Department of Anatomy and Embryology Faculty of Health, Medicine and Life Sciences, Maastricht University, Maastricht, The Netherlands. The samples were obtained from a female patient (82 years old) diagnosed with Alzheimer's disease, dementia, aphasia and depression. All methods were carried out in accordance with the relevant guidelines and regulations, and all experimental

protocols were approved by the Ethics Review Committee Psychology and Neuroscience. Brains were first fixed in situ by full-body perfusion via the femoral artery. Under a pressure of 0.2 bar, the body was perfused by 10 L of fixation fluid (1.8 vol% formaldehyde, 20% ethanol and 8.4% glycerine in water) within 1.5–2 hours. Thereafter, the body was preserved for at least 4 weeks for post-fixation submerged in the same fluid. Subsequently, brains were recovered by calvarial dissection and stored in 4% PFA in 0.1 M PBS until further processing. The samples were cleared and stained with MASH-AO as previously described<sup>22,33</sup>, with minor adjustments to the original protocol. The tissue was dehydrated in 20%, 40%, 60%, 80% and 100% MeOH in distilled water for 1 hour each at room temperature, followed by 1 hour in 100% MeOH and overnight bleaching in 5% H<sub>2</sub>O<sub>2</sub> in MeOH at 4 °C. Samples were then rehydrated in 80%, 60%, 40% and 20% MeOH and permeabilized two times for 1 hour in PBS containing 0.2% Triton X-100 (PBST). This was followed by a second bleaching step in freshly filtered 50% aqueous potassium disulfite solution. The samples were then thoroughly rinsed in distilled water five times and washed for another 1 hour. For staining, the samples were incubated in 0.001% acridine orange solution in McIlvaine buffer<sup>33</sup> (phosphate-citrate buffer) at pH 4 for 5 days at room temperature. After 2.5 days, the samples were flipped to allow for equal penetration of the dye from both sides. After staining, samples were washed two times for 1 hour in the same buffer solution, dehydrated in 20%, 40%, 60%, 80% and 2 × 100% MeOH for 1 hour each and delipidated in 66% DCM/33% MeOH overnight. These steps were followed by 2 × 1-hour washes in 100% DCM and immersion in ECI<sup>22,33</sup>.

### Reporting summary

Further information on research design is available in the Nature Portfolio Reporting Summary linked to this article.

### Data availability

Imaging datasets acquired with the Schmidt objective and with the mesoSPIM light-sheet microscope are available upon reasonable request.

### Code availability

mesoSPIM datasets were acquired using mesospim-control 1.7.2 (<https://github.com/mesoSPIM/mesoSPIM-control>), a custom open-source image acquisition software. Code for PSF analysis is available upon reasonable request.

### References

- Voigt, F. F., Chen, J. L., Krueppel, R. & Helmchen, F. A modular two-photon microscope for simultaneous imaging of distant cortical areas in vivo. in *Proceedings Volume 9329, Multiphoton Microscopy in the Biomedical Sciences XV* (Eds. Periasamy, A. et al.) (SPIE, 2015).
- Kim, D. H. et al. Pan-neuronal calcium imaging with cellular resolution in freely swimming zebrafish. *Nat. Methods* **14**, 1107–1114 (2017).
- Naert, T. et al. Deep learning is widely applicable to phenotyping embryonic development and disease. *Development* **148**, dev199664 (2021).
- Willsey, H. R. et al. Katanin-like protein Katnal2 is required for ciliogenesis and brain development in *Xenopus* embryos. *Dev. Biol.* **442**, 276–287 (2018).
- McIlvaine, T. C. A buffer solution for colorimetric comparison. *J. Biol. Chem.* **49**, 183–186 (1921).

### Acknowledgements

We would like to thank S. Giger for machining all custom objective parts, J. Kuhl for illustrations, D. Liittschwager for scallop photographs, B. Grewe for providing data acquisition hardware, U. Fuchs for optical design discussions, H. Kasper and M. Wieckhorst for technical assistance and S. Weidner for the design and production of 3D-printed parts. F.F.V. is supported by an HFSP fellowship (LTO0687).

T.N. received funding from H2020 Marie Skłodowska-Curie Actions (xenCAKUT - 891127). A.R. and S.H. were supported by a Dutch Science Foundation VIDI Grant (14637), and A.R. was additionally supported by an ERC Starting Grant (MULTICONNECT, 639938). In addition, this work was supported by the University Research Priority Program (URPP) 'Adaptive Brain Circuits in Development and Learning (AdaBD)' of the University of Zurich (E.S. and F.H.); grants from the Swiss National Science Foundation (grant nos. 31003B-170269, 310030\_192617 and CRSII5-18O316 to F.H. and 310030\_189102 to S.S.L.); an ERC Starting Grant by the European Union's Horizon 2020 Research and Innovation Programme to S.S.L (grant agreement no. 804474, DiRECT); and the US Brain Initiative (1U01NS090475-01, F.H.).

### Author contributions

F.F.V. and F.H. designed the project. F.F.V. designed the objective, built the microscope, imaged samples and analyzed data. A.M.R., T.N., S.H., M.S., A.L.H., A.B., S.C.F.N., A.R., E.T.S., S.S.L. and A.A. provided samples. L.W. created animations. F.F.V. and F.H. wrote the manuscript, with input from all coauthors.

### Funding

Open access funding provided by University of Zurich.

### Competing interests

F.F.V. and F.H. have filed a patent application (EP3893038A1) for the objective design. The remaining authors declare no competing interests.

### Additional information

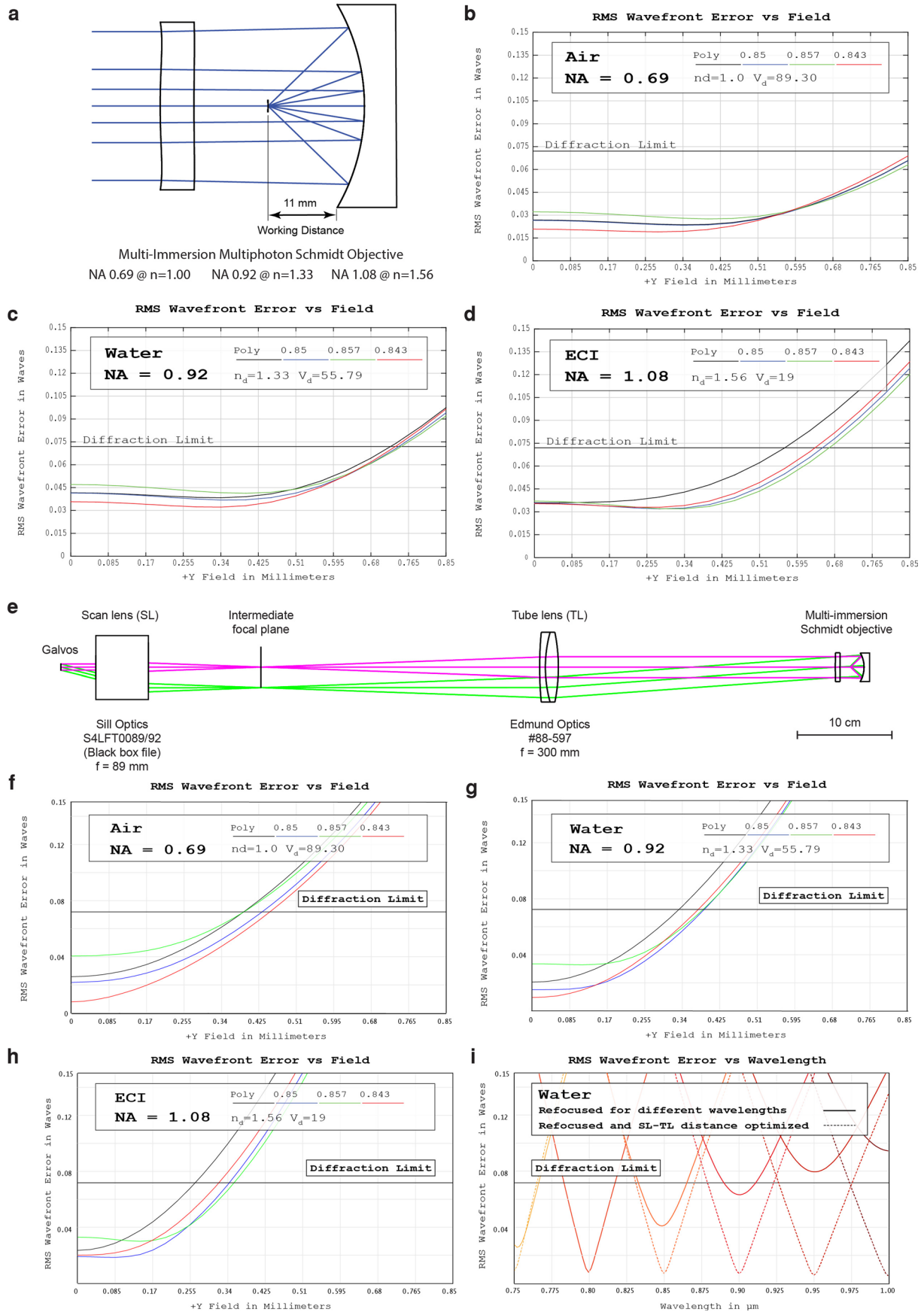
**Extended data** is available for this paper at <https://doi.org/10.1038/s41587-023-01717-8>.

**Supplementary information** The online version contains supplementary material available at <https://doi.org/10.1038/s41587-023-01717-8>.

**Correspondence and requests for materials** should be addressed to Fabian F. Voigt.

**Peer review information** *Nature Biotechnology* thanks Hiroki Ueda, Brad Amos, Qionghai Dai and the other, anonymous, reviewer(s) for their contribution to the peer review of this work.

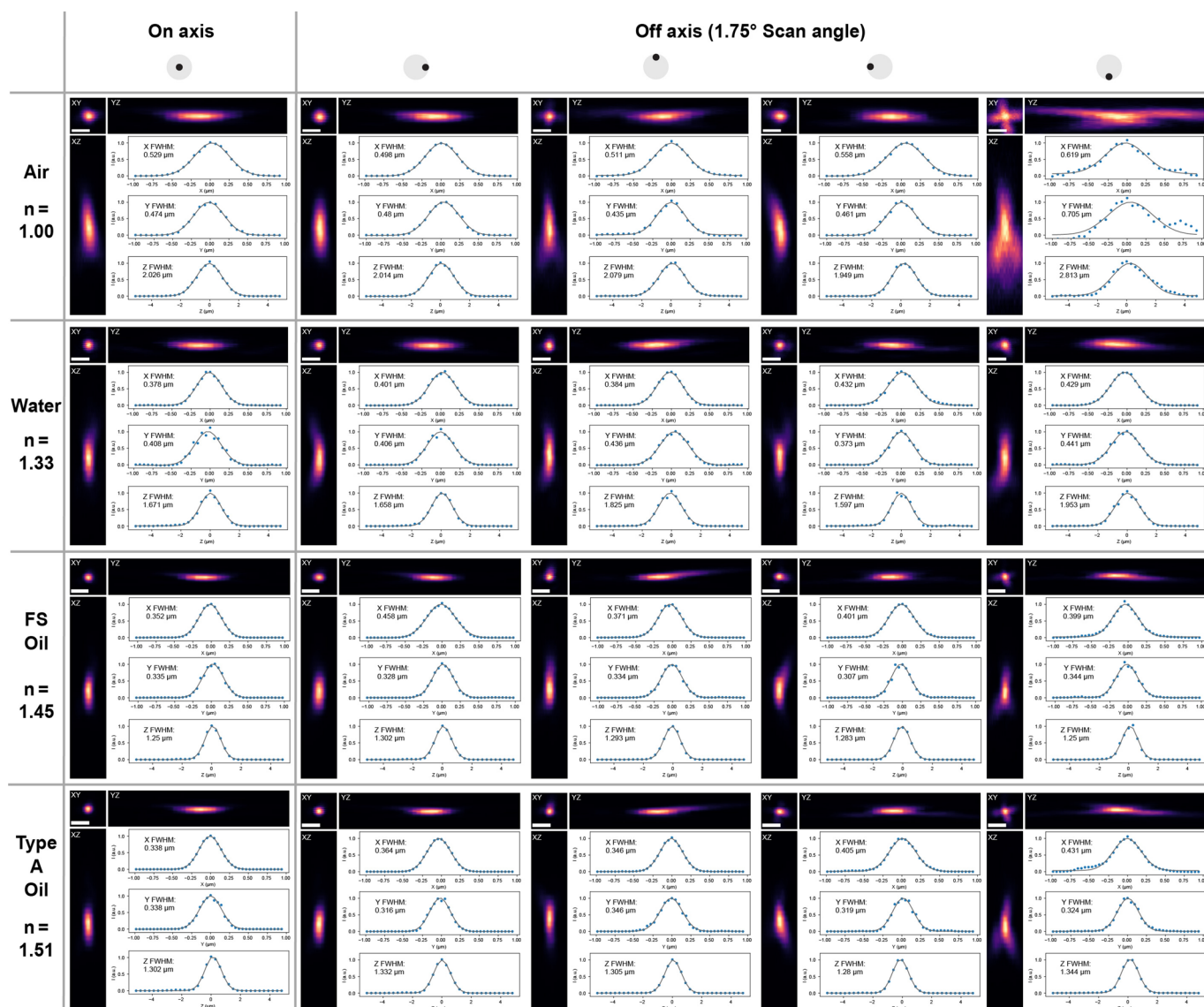
**Reprints and permissions information** is available at [www.nature.com/reprints](http://www.nature.com/reprints).



Extended Data Fig. 1 | See next page for caption.

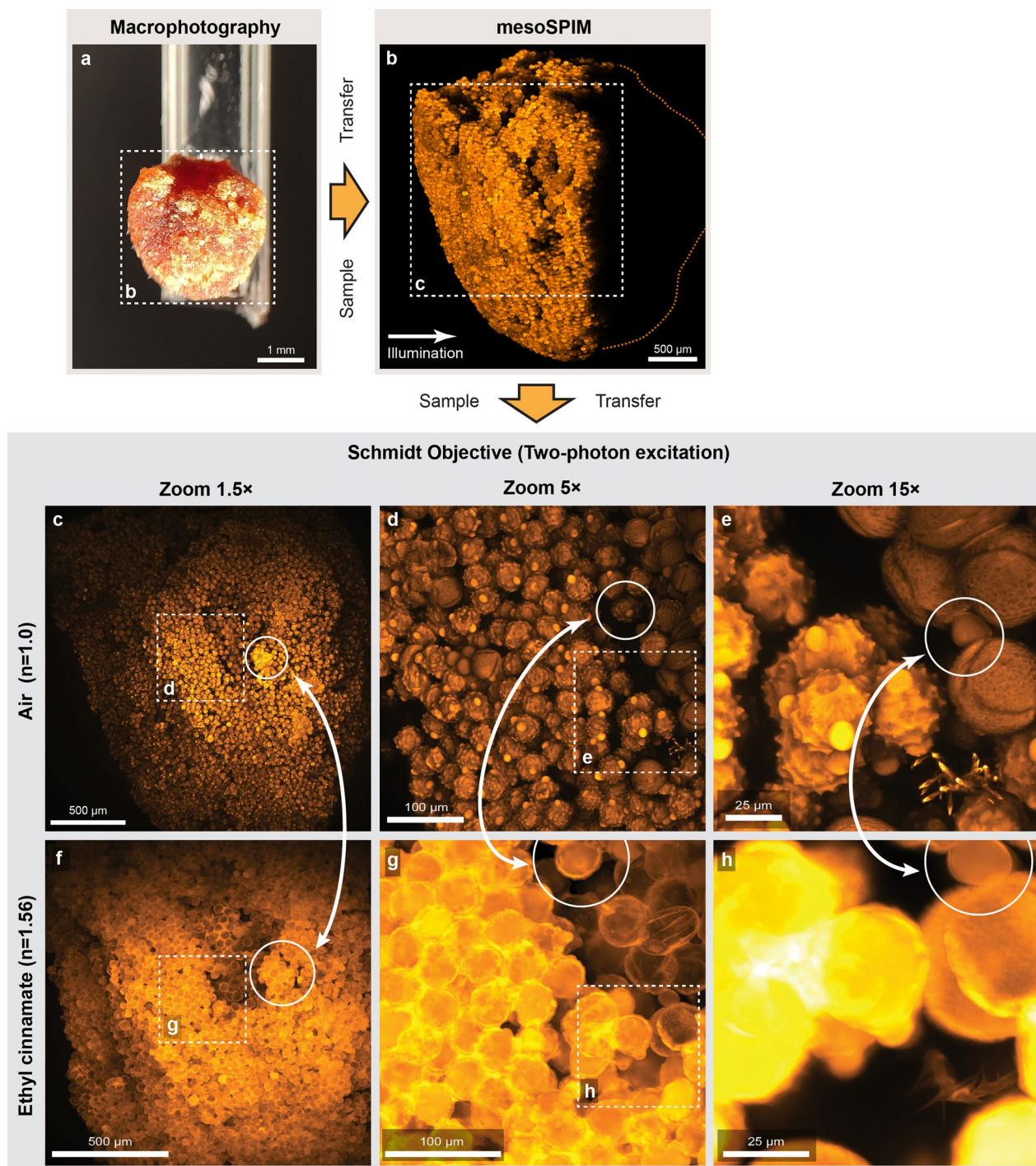
**Extended Data Fig. 1 | Theoretical performance of the Schmidt objective and the microscope. a)** Cross-section of the optical design. **b)–d)** Root-mean-square (RMS) wavefront aberration vs. FOV of the objective in air, water, ECI, respectively. **e)** Cross-section of the laser-scanning path. **f)–h)** Root-mean-square (RMS) wavefront aberration vs. FOV of the objective in air plus scan path, water,

ECI, respectively. Due to off-axis aberrations, the usable diffraction-limited FOV is reduced compared to the objective as a stand-alone item. **i)** On-axis RMS wavefront aberrations vs. wavelength. The system can be refocused to different wavelengths in the 750–1000 nm region. For best results, both the mirror-correction plate distance and the spacing of scan and tube lens can be optimized.



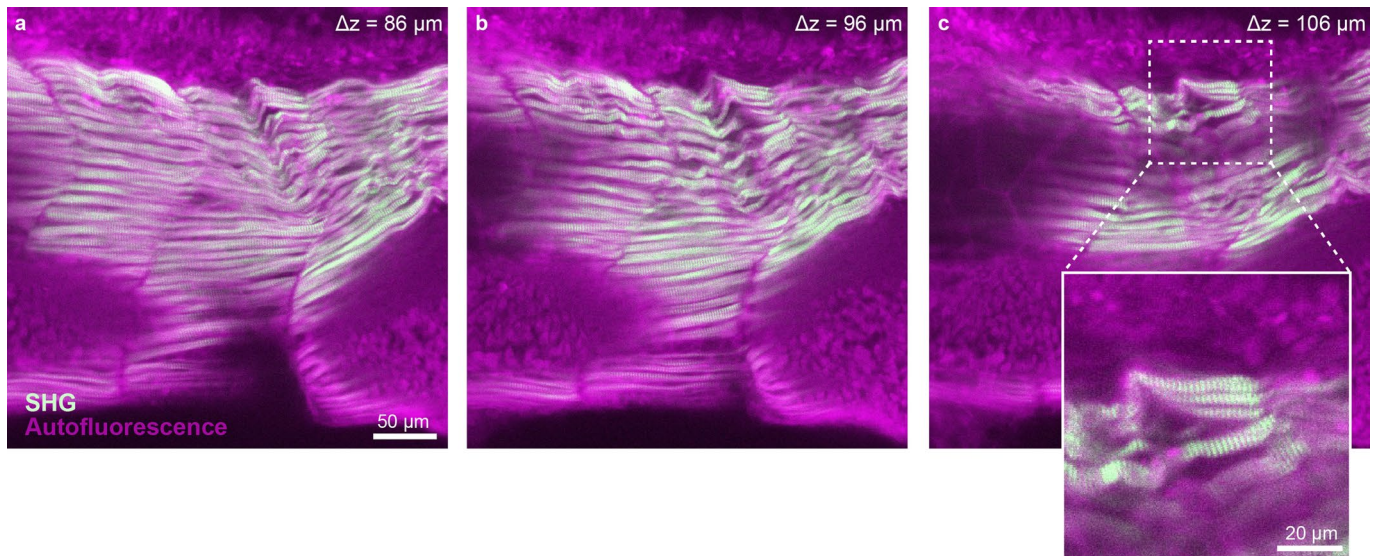
**Extended Data Fig. 2 | Example PSFs across the FOV in various media.** Shown are XYZ maximum projections of example PSFs taken at different FOV positions in different immersion media ranging from air and water to fused silica matching oil (FS Oil, Cargille 50350), and Type A oil (Cargille 16482). In general, the PSF size decreases with index as the increased NA leads to higher resolution. However,

beyond  $n = 1.45$ , there is no change in resolution. We attribute this to residual aberrations from the minimally refractive inner surface of the correction plate: As the correction plate is made of fused silica with  $n = 1.45$ , manufacturing-related surface irregularities have no effect at this index. Scale bar: 1  $\mu\text{m}$ .

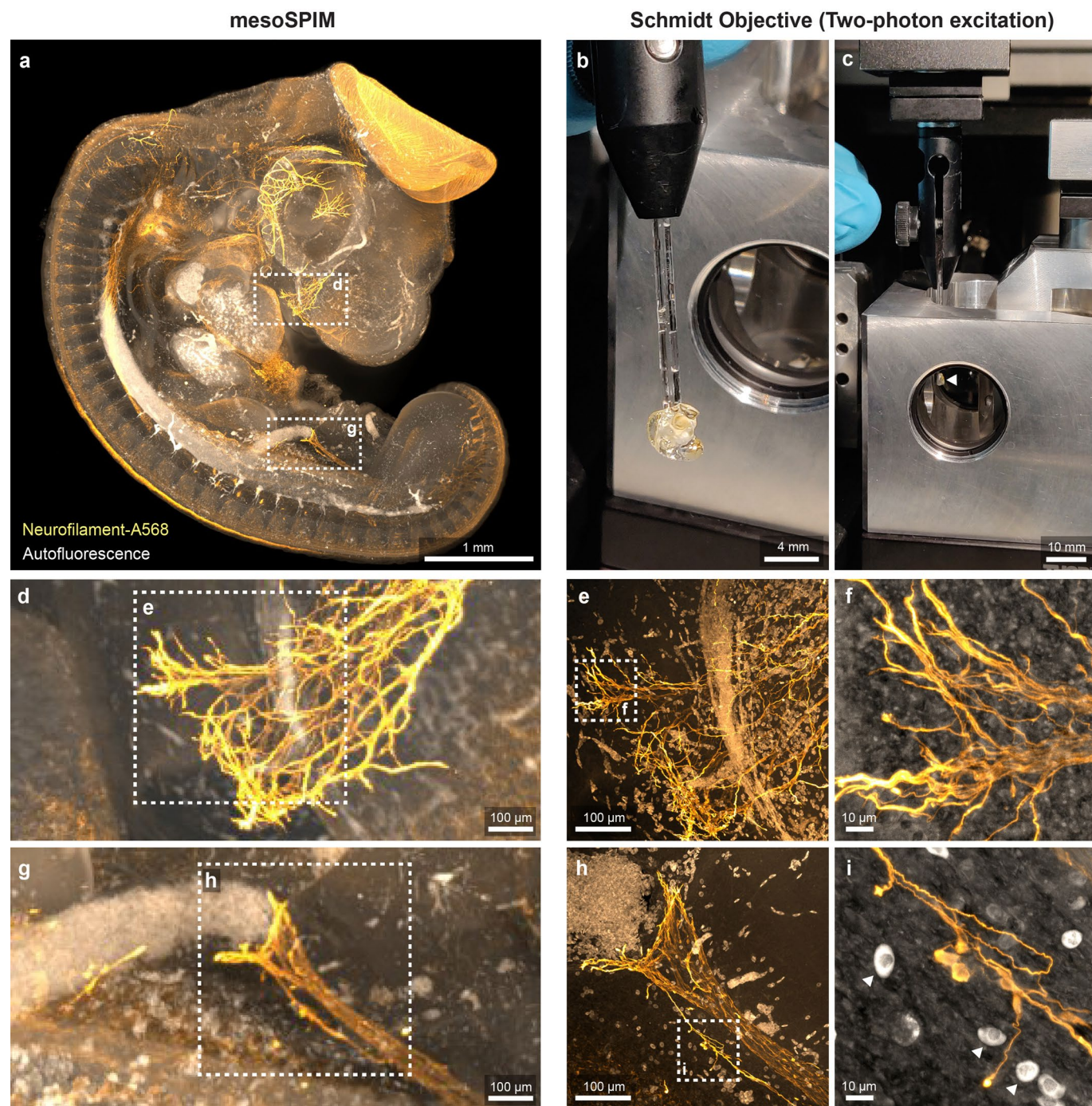


**Extended Data Fig. 3 | Imaging the same sample in air and in ethyl cinnamate (ECI).** **a**) A pollen pellet composed of many individual pollen grains. **b**) Maximum projection of a single-photon light-sheet (mesoSPIM) stack of the sample. As the sample was illuminated from the side, only part of the pollen pellet is visible. **c**) Maximum projection of a stack taken in air after transferring the sample into the Schmidt objective. **d**)–**e**) Maximum projections of stacks taken at higher zoom. **f**) The immersion chamber was then filled with ethyl cinnamate (ECI)

with an index of 1.56. This has several consequences: Firstly, at the same zoom level, the FOV shrinks by 1.56× as in the Schmidt objective, the product  $NA \times FOV$  is constant. Secondly, the pollen are now much better index-matched and the microscope can also start visualizing the interior of the pollen grains. Therefore, the visual appearance of pollen grains is different than in air. **g**)–**h**) Zoomed-in maximum projections. Similar sample regions in both images are highlighted with arrows. The experiment was repeated once.



**Extended Data Fig. 4 | SHG imaging with the Schmidt objective.** An unstained *Xenopus* embryo was embedded in Agarose and cleared using BABB. **a)–c)** Single z-planes from a stack taken in the tail of the tadpole in the sagittal plane highlighting SHG signal from muscles. The images are examples from one of four imaged tadpoles.

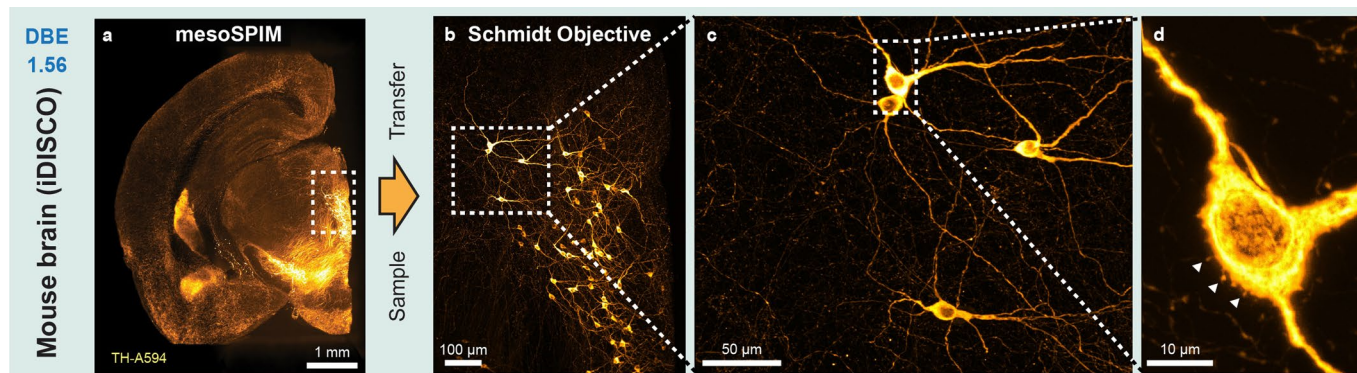


**Extended Data Fig. 5 | Correlative imaging of a 4-day old Chicken embryo with the mesoSPIM light-sheet microscope and the Schmidt objective.**

A chicken embryo was stained for Neurofilament using Alexa 568 as a secondary antibody and cleared using BABB. **a)** Maximum projection of a single photon light-sheet (mesoSPIM) overview dataset of the sample. **b)** Sample (glued to a glass capillary) prior to insertion into the Schmidt objective. **c)** Sample (white arrow) inserted into the Schmidt objective. **d) & g)** Maximum projections

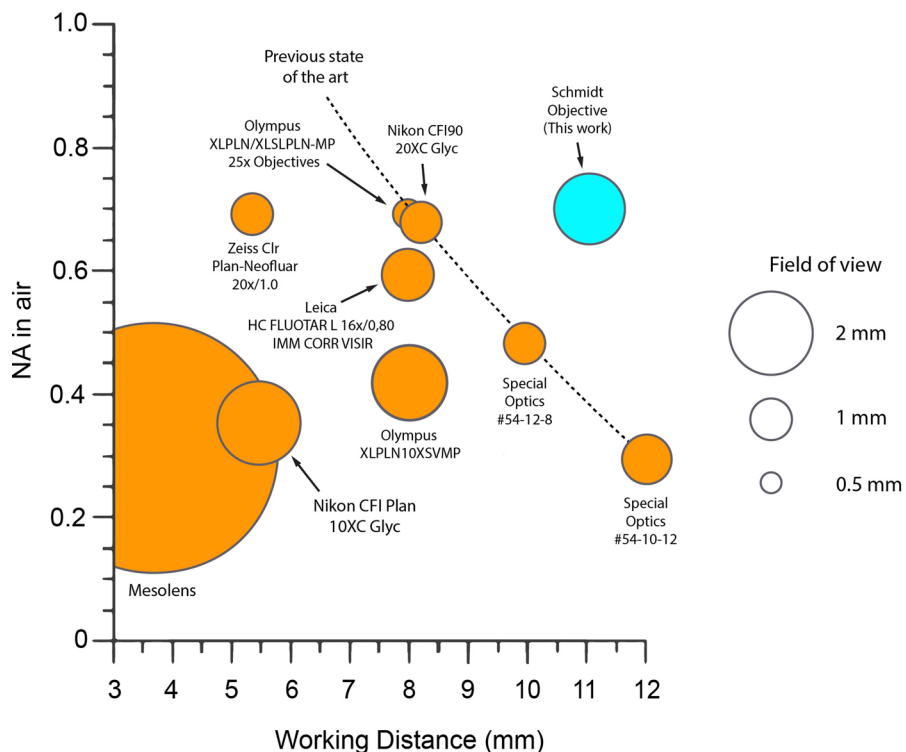
(mesoSPIM dataset) of a region of interest chosen for high-resolution imaging. **e) & h)** Maximum projections of z-stacks taken at the highlighted locations in **d) & g)** using the Schmidt objective and two-photon excitation. **f) & i)** Maximum projections of stacks taken at higher zoom level showing individual axons. The white cells with strong autofluorescence are red blood cells which have not lost their nucleus yet at this developmental stage. The images are examples from one of two imaged chicken embryos.





**Extended Data Fig. 6 | Dopaminergic neurons in the mouse brain imaged with the Schmidt objective.** A 5 mm-thick coronal slice of a mouse brain was stained for Tyrosine Hydroxylase (TH) using Alexa 594 as a secondary antibody and cleared using dibenzyl ether (DBE). **a**) Maximum projection of a single photon light-sheet (mesoSPIM) overview dataset of the sample. **b**) Maximum projection

of a z-stacks taken at the highlighted location in **a**) using the Schmidt objective and two-photon excitation at 800 nm. **c**) & **d**) Maximum projections of stacks taken at higher zoom level showing individual dopaminergic neurons and spines on the cell body of a neuron (arrows). The images are examples from one of two imaged brain slices.



**Extended Data Fig. 7 | Comparison of multi-immersion microscope objectives for multiphoton imaging.** In order to compare objectives with different index ranges, NA in air and working distance are used as a comparison metric. Only objectives with working distances larger than 3 mm are included in

this comparison. The field of view is the theoretical FOV based on simulations or the field number provided by the manufacturers. Among the listed microscope objectives, the Schmidt objective design is the only one that will actually deliver a diffraction-limited image in air.

## Reporting Summary

Nature Portfolio wishes to improve the reproducibility of the work that we publish. This form provides structure for consistency and transparency in reporting. For further information on Nature Portfolio policies, see our [Editorial Policies](#) and the [Editorial Policy Checklist](#).

### Statistics

For all statistical analyses, confirm that the following items are present in the figure legend, table legend, main text, or Methods section.

n/a | Confirmed

- The exact sample size ( $n$ ) for each experimental group/condition, given as a discrete number and unit of measurement
- A statement on whether measurements were taken from distinct samples or whether the same sample was measured repeatedly
- The statistical test(s) used AND whether they are one- or two-sided  
*Only common tests should be described solely by name; describe more complex techniques in the Methods section.*
- A description of all covariates tested
- A description of any assumptions or corrections, such as tests of normality and adjustment for multiple comparisons
- A full description of the statistical parameters including central tendency (e.g. means) or other basic estimates (e.g. regression coefficient) AND variation (e.g. standard deviation) or associated estimates of uncertainty (e.g. confidence intervals)
- For null hypothesis testing, the test statistic (e.g.  $F$ ,  $t$ ,  $r$ ) with confidence intervals, effect sizes, degrees of freedom and  $P$  value noted  
*Give  $P$  values as exact values whenever suitable.*
- For Bayesian analysis, information on the choice of priors and Markov chain Monte Carlo settings
- For hierarchical and complex designs, identification of the appropriate level for tests and full reporting of outcomes
- Estimates of effect sizes (e.g. Cohen's  $d$ , Pearson's  $r$ ), indicating how they were calculated

*Our web collection on [statistics for biologists](#) contains articles on many of the points above.*

### Software and code

Policy information about [availability of computer code](#)

Data collection	ScanImage 2017b12 (Vidrio Technologies) running on MATLAB 326 2019b (MathWorks) was used to control multi-photon image acquisition with the Schmidt objective. mesoSPIM datasets were acquired using mesospim-control 1.7.2 ( <a href="https://github.com/mesoSPIM/mesoSPIM-control">https://github.com/mesoSPIM/mesoSPIM-control</a> ), a custom open-source image acquisition software.
Data analysis	Data preprocessing (conversion to .tif, cropping, downsampling etc) was done using Fiji (fiji-2.0.0-pre-7). Volume renderings were generated with Imaris 9.6.0 (Bitplane) and exported supplemental videos were edited with Premiere Pro CC 2021 (Adobe). PSF datasets were analysed using Python 3.8.0 and napari 0.4.16. Calcium imaging datasets were analysed using suite2p v0.10.0 ( <a href="https://github.com/MouseLand/suite2p">https://github.com/MouseLand/suite2p</a> ).

For manuscripts utilizing custom algorithms or software that are central to the research but not yet described in published literature, software must be made available to editors and reviewers. We strongly encourage code deposition in a community repository (e.g. GitHub). See the Nature Portfolio [guidelines for submitting code & software](#) for further information.

## Data

Policy information about [availability of data](#)

All manuscripts must include a [data availability statement](#). This statement should provide the following information, where applicable:

- Accession codes, unique identifiers, or web links for publicly available datasets
- A description of any restrictions on data availability
- For clinical datasets or third party data, please ensure that the statement adheres to our [policy](#)

The data that support the findings of this study are available from the corresponding author upon request.

## Human research participants

Policy information about [studies involving human research participants and Sex and Gender in Research](#).

Reporting on sex and gender	The sample was obtained from a female patient.
Population characteristics	The patient (Age: 82 years) was diagnosed with Alzheimer's disease, dementia, aphasia, and depression.n/a
Recruitment	The human occipital lobe samples were obtained from the body donation program of the Department of Anatomy and Embryology, Maastricht University. The tissue donor gave their informed and written consent to the donation of their body for teaching and research purposes as regulated by the Dutch law for the use of human remains for scientific research and education ("Wet op de Lijkbezorging"). Accordingly, a handwritten and signed codicil from the donor posed when still alive and well, is kept at the Department of Anatomy and Embryology Faculty of Health, Medicine and Life Sciences, Maastricht University, Maastricht, The Netherlands.
Ethics oversight	All methods were carried out in accordance with the relevant guidelines and regulations and all experimental protocols were approved by the Ethics Review Committee Psychology and Neuroscience (ERCPN).

Note that full information on the approval of the study protocol must also be provided in the manuscript.

## Field-specific reporting

Please select the one below that is the best fit for your research. If you are not sure, read the appropriate sections before making your selection.

Life sciences  Behavioural & social sciences  Ecological, evolutionary & environmental sciences

For a reference copy of the document with all sections, see [nature.com/documents/nr-reporting-summary-flat.pdf](https://nature.com/documents/nr-reporting-summary-flat.pdf)

## Life sciences study design

All studies must disclose on these points even when the disclosure is negative.

Sample size	We did not calculate sample sizes beforehand. Regarding resolution measurements: Microscope point spread-functions are highly reproducible as they are caused by deterministic physical processes such as wavefront propagation and aberrations. Therefore, typical publications estimate PSFs with small sample sizes. To estimate PSF parameters reliably over the full FOV (equivalent to zoom 1), we chose the bead concentration such that 8 beads could be measured across sub-FOVs acquired using zoom 40.
Data exclusions	Only PSFs from beads surrounded by a bead-free window of 2 x 2 x 5 microns (X x Y x Z) were included in the analysis.
Replication	Fitting a PSF (for FWHM estimation) to each individual bead represents an individual measurement.
Randomization	We chose random subregions of the test samples (cover slips coated with beads) for PSF measurements.
Blinding	As the person analyzing the bead data was the same who took the data, blinding was not possible.

## Reporting for specific materials, systems and methods

We require information from authors about some types of materials, experimental systems and methods used in many studies. Here, indicate whether each material, system or method listed is relevant to your study. If you are not sure if a list item applies to your research, read the appropriate section before selecting a response.

## Materials &amp; experimental systems

n/a	Included in the study
<input type="checkbox"/>	<input checked="" type="checkbox"/> Antibodies
<input checked="" type="checkbox"/>	<input type="checkbox"/> Eukaryotic cell lines
<input checked="" type="checkbox"/>	<input type="checkbox"/> Palaeontology and archaeology
<input type="checkbox"/>	<input checked="" type="checkbox"/> Animals and other organisms
<input checked="" type="checkbox"/>	<input type="checkbox"/> Clinical data
<input checked="" type="checkbox"/>	<input type="checkbox"/> Dual use research of concern

## Methods

n/a	Included in the study
<input checked="" type="checkbox"/>	<input type="checkbox"/> ChIP-seq
<input checked="" type="checkbox"/>	<input type="checkbox"/> Flow cytometry
<input checked="" type="checkbox"/>	<input type="checkbox"/> MRI-based neuroimaging

## Antibodies

## Antibodies used

Mouse anti-neurofilament (RMO270, Invitrogen 13-0700)  
 Polyclonal rabbit-anti-tyrosine hydroxylase antibody (Sigma Aldrich, AB152)  
 Polyclonal chicken-anti-GFP antibody (Aves Labs, GFP-1020)  
 Donkey-anti-rabbit-AlexaFluor594 antibody (ThermoFisher, A32754)  
 Donkey-anti-chicken-AlexaFluor594 antibody (Jackson Immuno Research, 703-585-155)  
 Atp1a1 antibody (DSHB, A5)  
 Alexa Fluor-594 antibody (ThermoFisher A32742)  
 Goat anti-mouse IgG-Alexa 568 (Jackson ImmunoResearch 115-165-003)

## Validation

Antibody validation information for the Invitrogen 13-0700 mouse anti-neurofilament antibody is available from Thermo-Fisher Scientific under the Catalog-Number #13-0700. Validation information for the Sigma-Aldrich AB152 13-0700 and DSHB Atp1a1 antibody is available from the Sigma-Aldrich and DSHB, respectively.

## Animals and other research organisms

Policy information about [studies involving animals](#); [ARRIVE guidelines](#) recommended for reporting animal research, and [Sex and Gender in Research](#)

## Laboratory animals

elavl3:GCaMP6s zebrafish larvae, 5 days old.  
 C57BL6/J 363 wildtype and Thy1-YFP HJrs/J transgenic (Jackson, 003782) mice aged 4-17 weeks.  
 Xenopus tropicalis tadpoles, 4 days old

## Wild animals

The study did not involve any wild animals.

## Reporting on sex

The study used female mice. Sex of zebrafish and xenopus larvae can not be determined during the early stages we imaged.

## Field-collected samples

The study did not involve any field-collected samples.

## Ethics oversight

Cantonal Veterinary Office of the Canton of Zurich

Note that full information on the approval of the study protocol must also be provided in the manuscript.